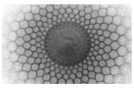
TTMP vol 3 (4), 2026
doi: 10.30511/TTMP.2026.2108620.1101

Transactions in Theoretical and Mathematical Physics



Analytical, Numerical, and PINN Analysis of the ABC Fractional GK Equation: A Compatibility-Aware Benchmark Study

Md. Akher Chowdhury[1], **Md. Masudar Rahman**[2,a], **Md. Zahangir Alam**[2], **Md. Ashik Iqbal**[3]

[1]Department of Mathematics, Begum Rokeya University, Rangpur-5404, Bangladesh
[2]Department of Mathematics, Bangladesh Army University of Engineering & Technology, Natore, Bangladesh
[3]Department of Applied Mathematics, University of Rajshahi, Rajshahi-6205, Bangladesh

Received: 11 Ocotber 2026 / Accepted: 10 November 2026 / Published: 14 November 2026

Abstract We develop a framework for comparing analytical, numerical, and machine-learning solutions of a time-fractional Gardner–Kawahara (GK) equation with the Atangana–Baleanu derivative in the Caputo sense (ABC). We construct a forced benchmark in which the nonlocal Mittag–Leffler (ML) memory law, the prescribed initial state, and the source term are compatible at the initial time. We solve the same benchmark using three approaches: a Laplace–Adomian decomposition method (LADM), a Fourier pseudospectral discretization with an AB predictor–corrector scheme for the history term, and a physics-informed neural network (PINN) based on the equivalent Atangana–Baleanu integral equation.

We assess the six-component LADM approximation over the selected short-time interval. At the lowest fractional order considered, the last retained component is less than 1% of the total solution, and the normalized integral residual is approximately 3.10×10^{-3}. The numerical solution exhibits coarse-to-refined relative differences of order 10^{-8} to 10^{-7}. At $t = 0.10$, the relative L_2 error between the numerical and LADM solutions ranges from 4.42×10^{-8} for $\alpha = 1.00$ to 2.92×10^{-3} for $\alpha = 0.85$. For $\alpha = 0.90$, the PINN reproduces the numerical wave field with relative L_2 errors of 1.07% over the full space–time domain and 1.26% at the final time.

Both the LADM and numerical solutions show that decreasing the fractional order strengthens the forced transient response in this benchmark. The benchmark provides a reproducible setting for cross-validating semi-analytical decomposition, spectral computation, and physics-informed learning for the ABC fractional GK equation.

Keywords: Gardner-Kawahara equation; Laplace Adomian decomposition; Fourier pseudo spectral; predictor-corrector method; physics-informed neural network

1 Introduction

Fractional calculus extends differentiation and integration from integer orders to non-integer orders and provides a mathematical language for systems with hereditary effects, anomalous transport, long-range temporal dependence, and nonlocal constitutive behaviour [1–4]. Based on the Riemann–Liouville and Caputo operators, classical fractional models have been widely used, but their power-law kernels are singular at the origin. The AB family of operators was proposed with a non-singular, nonlocal ML kernel, providing an alternative memory law that retains a Caputo-like treatment of initial data while avoiding a singular kernel [5, 6]. Numerical approximations and time-integration procedures for the AB derivative have since been developed for a variety of fractional differential equations [7–10].

[a]Corresponding author: masudarmath@gmail.com

The Kawahara equation is a fifth-order nonlinear dispersive evolution equation associated with oscillatory solitary waves, capillary–gravity wave propagation, and magneto-acoustic phenomena-related problems [11]. In near-critical interfacial-wave forms, the GK equation arises as a natural extension that combines quadratic and cubic nonlinearities with third- and fifth-order dispersion [12]. This combination makes the model substantially richer than the classical KdV, modified KdV, or Kawahara equations because the competing nonlinear and dispersive mechanisms can alter amplitude, polarity, oscillatory tails, and propagation structure.

A broad literature has addressed Kawahara-type equations by both the analytical and numerical techniques. The Adomian decomposition method has been used for classical and fractional Kawahara models [13–16], while AB memory has been introduced into a modified Kawahara equation and treated using a homotopy-analysis-transform framework [17]. Also, the exact or semi-analytical solutions have been developed for fractional Kawahara equations under conformable or Caputo-type formulations [18, 19]. For this type of GK equation, recent numerical studies have used high-order B-spline collocation and finite-element strategies [20, 21]. Fourier pseudo-spectral methods are also attractive for periodic, high-order dispersive equations because derivatives can be computed with spectral accuracy via fast Fourier transforms [22].

In parallel, physics-informed neural networks (PINNs) have emerged as a framework for embedding differential equations directly into neural-network training [23–26]. By incorporating history-dependent residuals, fractional PINNs extend this concept to nonlocal operators [24]. Recently, PINNs have been used for inverse GK parameter identification [27], and a dedicated PINN framework has been reported for modified Kawahara equations [28]. These developments establish the feasibility of learning high-order nonlinear wave dynamics, but they do not eliminate the need for independent analytical and numerical validation, particularly when a nonlocal fractional derivative is present.

A vital issue in ABC fractional evolution problems is the compatibility between the initial state and the local part of the associated AB integral operator. If a nonzero initial profile is combined with a spatial operator that is already nonzero at $t = 0$, a naive benchmark will exhibit an apparent start-up mismatch even when the algebraic derivation is otherwise correct. As a result, the present work adopts a zero initial state and a time-dependent forcing that vanishes at $t = 0$, which produces a nontrivial wave after the initial instant while preserving compatibility of the fractional model.

1.1 Novelty and contributions

The novelty of this paper lies in the combined formulation and validation strategy. In the literature reviewed for this study, individual works have considered ABC-modified Kawahara models [17], Caputo or conformable fractional Kawahara equations [15, 18, 19], classical GK numerical schemes [20, 21], and PINN formulations for classical Gardner–Kawahara or modified Kawahara equations [27, 28]. The reviewed studies do not provide the same combination of an ABC time-fractional GK equation containing both quadratic and cubic nonlinearities; an explicitly compatibility-aware forced benchmark; a Laplace–Adomian analytical approximation; an independent Fourier pseudo-spectral ABC history solver; and a PINN validated against the converged numerical field on the same benchmark.

Therefore, the study makes four connected contributions. First, it formulates a compatible forced ABC GK test problem that avoids the start-up inconsistency encountered with an incompatible nonzero initial state. Secondly, it constructs and validates a six-component LADM approximation for several fractional orders. Thirdly, it produces an independent grid-converged Fourier pseudo-spectral solution and uses it to quantify the truncation error of the analytical series. Lastly, it demonstrates that an integral-form PINN can recover the representative fractional wave field from the governing physics and constraints, thereby providing a three-way analytical-numerical-PINN assessment rather than a single-method demonstration. So, a further contribution is the consolidated cross-method visualization: fractional-order profiles, space-time surfaces, pairwise solution overlays, and absolute-error diagnostics are compared

under the same parameter set, so agreement is assessed visually and quantitatively rather than by a single error metric.

The remainder of the paper is organized as follows. In Section 2, we state the AB definitions used throughout the work. Section 3 gives the analytical, numerical, and PINN methodologies. Sections 4, 5, and 6 present the corresponding applications and results. Section 7 compares the three solution strategies. Section 8 positions the results relative to related studies. In Section 9, we give the main conclusions and future directions.

2 AB Fractional Definitions

Let $0 < \alpha \le 1$ and f be sufficiently smooth on $[0,T]$. The AB derivative in the Caputo sense is defined by [5, 6]

$$
\begin{aligned}
{}^{\mathrm{ABC}}D_t^{\alpha} f(t) = \frac{B(\alpha)}{1-\alpha}\int_0^t f'(\tau) \\
\times E_\alpha\left[-\frac{\alpha}{1-\alpha}(t-\tau)^{\alpha}\right]\mathrm{d}\tau,
\end{aligned}
\tag{1}
$$

where $E_\alpha(z)$ denotes the one-parameter ML function,

$$
E_\alpha(z) = \sum_{k=0}^{\infty} \frac{z^k}{\Gamma(\alpha k+1)}. \tag{2}
$$

The normalization function satisfies $B(0) = B(1) = 1$. In the present computations, we use the normalization

$$
B(\alpha) = 1-\alpha+\frac{\alpha}{\Gamma(\alpha)}, \tag{3}
$$

which is adopted consistently in the analytical, numerical, and PINN implementations. The Laplace transform of the ABC derivative can be written as

$$
\mathscr{L}\left\{{}^{\mathrm{ABC}}D_t^{\alpha} f(t)\right\}(s) = \frac{B(\alpha)}{1-\alpha}\frac{s^{\alpha}F(s)-s^{\alpha-1}f(0)}{s^{\alpha}+\alpha/(1-\alpha)}. \tag{4}
$$

The fractional integral associated with the AB operator is [5, 6]

$$
\begin{aligned}
{}^{\mathrm{AB}}I_t^{\alpha} f(t) = \frac{1-\alpha}{B(\alpha)} f(t) \\
+\frac{\alpha}{B(\alpha)\Gamma(\alpha)}\int_0^t (t-\tau)^{\alpha-1} f(\tau)\,\mathrm{d}\tau.
\end{aligned}
\tag{5}
$$

Equation (5) contains a local contribution and a history integral. This decomposition is central to all three methods used below. LADM applies it analytically, the numerical scheme approximates the history integral by product integration, and the PINN enforces the same integral relation through its physics loss.

3 Methodology

The general forced ABC fractional Gardner–Kawahara equation considered in this work is

$$
\begin{aligned}
{}^{\mathrm{ABC}}D_t^{\alpha} u + cu_x + auu_x - bu^2u_x \\
+\mu u_{xxx} + \nu u_{xxxxx} = S(x,t), \qquad 0 < \alpha \le 1.
\end{aligned}
\tag{6}
$$

We define the GK spatial operator by

$$
\mathscr{G}(u) = cu_x + auu_x - bu^2u_x + \mu u_{xxx} + \nu u_{xxxxx}. \tag{7}
$$

The evolution equation takes the compact form

$$
{}^{\mathrm{ABC}}D_t^{\alpha} u = S(x,t) - \mathscr{G}(u). \tag{8}
$$

Periodic spatial boundary conditions are used in the benchmark because they are naturally compatible with the Fourier discretization and the periodic forcing selected in Section 4.

3.1 Analytical Methodology: Laplace–Adomian Decomposition Method

Applying the Laplace transform in time to Eq. (16), using Eq. (4), and then inverting gives the equivalent AB integral equation

$$
\begin{aligned}
u(x,t) = \phi(x) + {}^{\mathrm{AB}}I_t^{\alpha}\left[S(x,t) - \mathscr{G}(u)\right], \\
\phi(x) = u(x,0).
\end{aligned}
\tag{9}
$$

The LADM solution is expanded as

$$
u(x,t) = \sum_{n=0}^{\infty} u_n(x,t), \tag{10}
$$

where the quadratic nonlinear term uu_x is decomposed into Adomian components

$$
A_n = \frac{1}{n!}\frac{\mathrm{d}^n}{\mathrm{d}\lambda^n}\left[\left(\sum_{k=0}^{\infty}\lambda^k u_k\right)\left(\sum_{k=0}^{\infty}\lambda^k u_{k,x}\right)\right]_{\lambda=0}, \tag{11}
$$

while the cubic-gradient term u^2u_x is written as

$$
C_n = \frac{1}{n!}\frac{\mathrm{d}^n}{\mathrm{d}\lambda^n}\left[\left(\sum_{k=0}^{\infty}\lambda^k u_k\right)^2\left(\sum_{k=0}^{\infty}\lambda^k u_{k,x}\right)\right]_{\lambda=0}. \tag{12}
$$

The nth decomposed spatial contribution is therefore

$$
G_n = cu_{n,x} + aA_n - bC_n + \mu u_{n,xxx} + \nu u_{n,xxxxx}. \tag{13}
$$

For a forced problem, the leading component is chosen as

$$u_0(x,t) = \phi(x) + {}^{\mathrm{AB}}I_t^{\alpha} S(x,t), \tag{14}$$

and the remaining components are generated recursively through

$$u_{n+1}(x,t) = -{}^{\mathrm{AB}}I_t^{\alpha} G_n(x,t), \qquad n = 0,1,2,\ldots. \tag{15}$$

After $M+1$ components, the analytical approximation is The evolution equation takes the compact form

$${}^{\mathrm{ABC}}D_t^{\alpha} u = S(x,t) - \mathscr{G}(u). \tag{16}$$

Periodic spatial boundary conditions are used in the benchmark because they are naturally compatible with the Fourier discretization and the periodic forcing selected in Section 4.

3.2 Analytical Methodology: Laplace–Adomian Decomposition Method

Applying the Laplace transform in time to Eq. (16), using Eq. (4), and then inverting gives the equivalent AB integral equation

$$\begin{aligned} u(x,t) &= \phi(x) + {}^{\mathrm{AB}}I_t^{\alpha}\left[S(x,t) - \mathscr{G}(u)\right], \\ \phi(x) &= u(x,0). \end{aligned} \tag{17}$$

The LADM solution is expanded as

$$u(x,t) = \sum_{n=0}^{\infty} u_n(x,t), \tag{18}$$

where the quadratic nonlinear term uu_x is decomposed into Adomian components

$$A_n = \frac{1}{n!}\frac{\mathrm{d}^n}{\mathrm{d}\lambda^n}\left[\left(\sum_{k=0}^{\infty}\lambda^k u_k\right)\left(\sum_{k=0}^{\infty}\lambda^k u_{k,x}\right)\right]_{\lambda=0}, \tag{19}$$

while the cubic-gradient term u^2u_x is written as

$$C_n = \frac{1}{n!}\frac{\mathrm{d}^n}{\mathrm{d}\lambda^n}\left[\left(\sum_{k=0}^{\infty}\lambda^k u_k\right)^2\left(\sum_{k=0}^{\infty}\lambda^k u_{k,x}\right)\right]_{\lambda=0}. \tag{20}$$

The nth decomposed spatial contribution is therefore

$$G_n = cu_{n,x} + aA_n - bC_n + \mu u_{n,xxx} + \nu u_{n,xxxxx}. \tag{21}$$

For a forced problem, the leading component is chosen as

$$u_0(x,t) = \phi(x) + {}^{\mathrm{AB}}I_t^{\alpha} S(x,t), \tag{22}$$

and the remaining components are generated recursively through

$$u_{n+1}(x,t) = -{}^{\mathrm{AB}}I_t^{\alpha} G_n(x,t), \qquad n = 0,1,2,\ldots. \tag{23}$$

After $M+1$ components, the analytical approximation is

$$u_{\mathrm{LADM}}^{(M)}(x,t) = \sum_{n=0}^{M} u_n(x,t). \tag{24}$$

The convergence assessment in Section 4 is based on the relative size of the last retained component, preservation of the initial condition, and substitution of the truncated series into the integral equation. The AB integral form is particularly useful because it avoids direct numerical evaluation of the ML kernel during the LADM recursion.

3.3 Numerical Methodology: Fourier Pseudo-spectral ABC Predictor–Corrector Scheme

On the periodic spatial interval $[-\pi,\pi]$, we introduce a uniform Fourier grid,

$$\begin{aligned} x_j &= -\pi + j\Delta x, \qquad \Delta x = \frac{2\pi}{N_x}, \\ & j = 0,1,\ldots,N_x-1, \end{aligned} \tag{25}$$

and discretize the time interval as

$$t_n = n\Delta t, \qquad \Delta t = \frac{T}{N_t}, \quad n = 0,1,\ldots,N_t. \tag{26}$$

If $\widehat{U}(k,t)$ denotes the discrete Fourier transform of the nodal vector $U(t)$, then the mth spatial derivative is evaluated spectrally by

$$D_x^m U = \mathscr{F}^{-1}\left[(\mathrm{i}k)^m \widehat{U}\right]. \tag{27}$$

A two-thirds de-aliasing filter is applied to nonlinear products to reduce aliasing contamination. After spatial discretization, Eq. (16) becomes the fractional system

$$\begin{aligned} {}^{\mathrm{ABC}}D_t^{\alpha} U(t) &= F(U,t) \\ &= S(t) - \mathscr{G}_h(U). \end{aligned} \tag{28}$$

Using Eq. (5), the discrete history contribution is constructed by product-linear integration. Let

$$\delta_m^{(\alpha)} = (m+1)^{\alpha} - m^{\alpha}. \tag{29}$$

The linear-interpolation weights used over each past subinterval are

$$A_m = \frac{(m+1)^{\alpha+1} - m^{\alpha+1}}{\alpha+1} - \frac{m\,\delta_m^{(\alpha)}}{\alpha}, \tag{30}$$

and

$$B_m = \frac{(m+1)\delta_m^{(\alpha)}}{\alpha} - \frac{(m+1)^{\alpha+1} - m^{\alpha+1}}{\alpha+1}. \tag{31}$$

At each new time level, the memory integral is approximated by a weighted sum of previous right-hand-side values. A predictor is first formed from the known history, and a corrected value is then obtained by re-evaluating the nonlinear terms. In Fourier space, the stiff third- and fifth-order linear dispersive contributions are treated semi-implicitly, while the nonlinear terms are updated by fixed-point iteration. This separation reduces the severe time-step restriction that would otherwise arise from the fifth-order derivative. The solver thus combines spectral differentiation in space, AB history quadrature in time, and a semi-implicit corrector. The numerical method is validated in two independent ways, by comparison with the LADM solution and by a grid-refinement test. The refined numerical field is subsequently used as the principal reference for PINN assessment.

3.4 Physics-Informed Neural Network Methodology

The PINN approximates the solution by a neural function $u_\theta(x,t)$, where θ denotes all trainable weights and biases. On the periodic spatial domain, the coordinate x is encoded through $\sin x$ and $\cos x$, so that periodicity is built into the network representation:

$$u_\theta(x,t) = \mathscr{N}_\theta(\sin x, \cos x, t). \tag{32}$$

To avoid repeatedly evaluating the ML derivative, the PINN enforces the equivalent AB integral equation. We define

$$\begin{aligned} F_\theta = S(x,t) - \big[&c(u_\theta)_x + a u_\theta (u_\theta)_x \\ &- b u_\theta^2 (u_\theta)_x + \mu (u_\theta)_{xxx} + \nu (u_\theta)_{xxxxx}\big]. \end{aligned} \tag{33}$$

The spatial derivatives are obtained by automatic differentiation. The physics residual is then

$$\begin{aligned} R_\theta = u_\theta - \phi(x) &- \frac{1-\alpha}{B(\alpha)} F_\theta \\ &- \frac{\alpha}{B(\alpha)\Gamma(\alpha)} \int_0^t (t-\tau)^{\alpha-1} F_\theta(x,\tau)\,\mathrm{d}\tau. \end{aligned} \tag{34}$$

The history integral is discretized on ordered time levels using the same class of product-integration weights as in Section 3.2. With a characteristic solution scale U_s, the normalized physics loss is

$$\mathscr{L}_f = \frac{1}{N_f} \sum_{i=1}^{N_f} \left| \frac{R_\theta(x_i,t_i)}{U_s} \right|^2. \tag{35}$$

When the initial condition is enforced softly, the total loss may include an additional initial-condition term. In the present implementation, the initial condition is imposed as a hard output constraint. Its contribution to the training loss is therefore identically zero, and the optimized objective is the fractional physics residual loss.

4 Analytical Application and Results

We now apply the analytical formulation to a compatibility-aware forced ABC fractional GK benchmark. The source term is selected to vanish at the initial time so that the zero initial state, the local part of the AB integral, and the spatial operator are mutually consistent.

4.1 Selected Compatible Test Problem

The benchmark equation is

$$\begin{aligned} {}^{\mathrm{ABC}}D_t^\alpha u + 2u_x + \frac{5}{7} u u_x - \frac{15}{7} u^2 u_x \\ + \frac{1}{3} u_{xxx} + \frac{1}{42} u_{xxxxx} = t \sin x. \end{aligned} \tag{36}$$

The computational domain is

$$-\pi \le x \le \pi, \qquad 0 \le t \le 0.10. \tag{37}$$

The initial condition is

$$u(x,0) = 0, \tag{38}$$

and periodic boundary conditions are imposed:

$$\begin{aligned} &u(-\pi,t) = u(\pi,t), \\ &\partial_x^m u(-\pi,t) = \partial_x^m u(\pi,t), \qquad m = 1,2,\ldots,5. \end{aligned} \tag{39}$$

The fixed parameters are

$$\begin{aligned} &c = 2, \qquad a = \frac{5}{7}, \qquad b = \frac{15}{7}, \\ &\mu = \frac{1}{3}, \qquad \nu = \frac{1}{42}. \end{aligned} \tag{40}$$

The fractional orders considered are

$$\alpha = 1.00, \quad 0.95, \quad 0.90, \quad 0.85. \tag{41}$$

At $t = 0$, the solution and all its spatial derivatives vanish, and the forcing $t \sin x$ is also zero. The initial state is therefore compatible with the governing equation and its AB integral representation.

4.2 LADM Application

Since the initial state is zero, the leading LADM component is generated entirely by the forcing:

$$u_0(x,t) = {}^{\mathrm{AB}}I_t^{\alpha}[t \sin x]. \tag{42}$$

Using Eq. (5), we obtain

$$u_0(x,t) = \sin x \left[\frac{1-\alpha}{B(\alpha)} t + \frac{\alpha}{B(\alpha)\Gamma(\alpha+2)} t^{\alpha+1} \right]. \tag{43}$$

For $\alpha = 1$, this reduces to

$$u_0(x,t) = \frac{t^2}{2} \sin x. \tag{44}$$

The higher components are generated as follows:

$$u_1 = -{}^{\mathrm{AB}}I_t^{\alpha}[G_0], \tag{45}$$

$$u_2 = -{}^{\mathrm{AB}}I_t^{\alpha}[G_1], \tag{46}$$

and, in general,

$$u_{n+1} = -{}^{\mathrm{AB}}I_t^{\alpha}[G_n]. \tag{47}$$

Six components, u_0 through u_5, are retained. The final analytical approximation is therefore

$$u_{\mathrm{LADM}}^{(5)}(x,t) = \sum_{n=0}^{5} u_n(x,t). \tag{48}$$

4.3 Analytical Evaluation and Validation

The relative magnitude of the final retained component is measured by

$$\eta_5 = \frac{\|u_5\|_2}{\|u_{\mathrm{LADM}}^{(5)}\|_2}. \tag{49}$$

Initial-condition consistency is checked at a small positive time ε through

$$E_{\mathrm{IC}} = \max_x \left| u_{\mathrm{LADM}}^{(5)}(x,\varepsilon) \right|. \tag{50}$$

The integral-equation residual is

$$R_I = u_{\mathrm{LADM}}^{(5)} - {}^{\mathrm{AB}}I_t^{\alpha} \left[t \sin x - \mathscr{G}\left(u_{\mathrm{LADM}}^{(5)} \right) \right], \tag{51}$$

with normalized measure

$$E_R = \frac{\|R_I\|_2}{\|u_{\mathrm{LADM}}^{(5)}\|_2}. \tag{52}$$

Table 1 Validation of the six-component LADM approximation at $t = 0.10$.

α	η_5	Relative residual	Maximum IC error
1.00	$5.48562432 \times 10^{-8}$	$1.15874427 \times 10^{-9}$	$5.00000000 \times 10^{-17}$
0.95	$8.34878532 \times 10^{-5}$	$1.15016034 \times 10^{-5}$	$5.12977160 \times 10^{-10}$
0.90	$1.32648851 \times 10^{-3}$	$3.30414648 \times 10^{-4}$	$1.04469768 \times 10^{-9}$
0.85	$8.47731817 \times 10^{-3}$	$3.10022266 \times 10^{-3}$	$1.58203849 \times 10^{-9}$

At $t = 0.10$, the last retained component contributes less than 1% of the accumulated solution magnitude even for $\alpha = 0.85$. The normalized residual is approximately 0.31% in that case, and the initial-condition diagnostic remains below 1.6×10^{-9} for all the fractional cases.

Figure 1 shows a systematic increase in the forced response as the fractional order decreases from 1.00 to 0.85. With the forcing and coefficients held fixed, the larger amplitude reflects the change in the transient response under the ABC memory law. The profiles also exhibit a modest spatial shift and a change in shape, indicating that memory interacts with both nonlinearity and higher-order dispersion.

Figure 2 shows the evolution of the $\alpha = 0.90$ solution from the zero initial state. The wave amplitude grows under

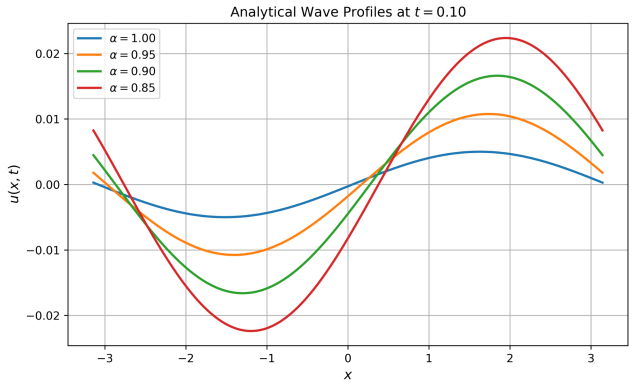


Fig. 1 Analytical LADM wave profiles for different fractional orders at $t = 0.10$.

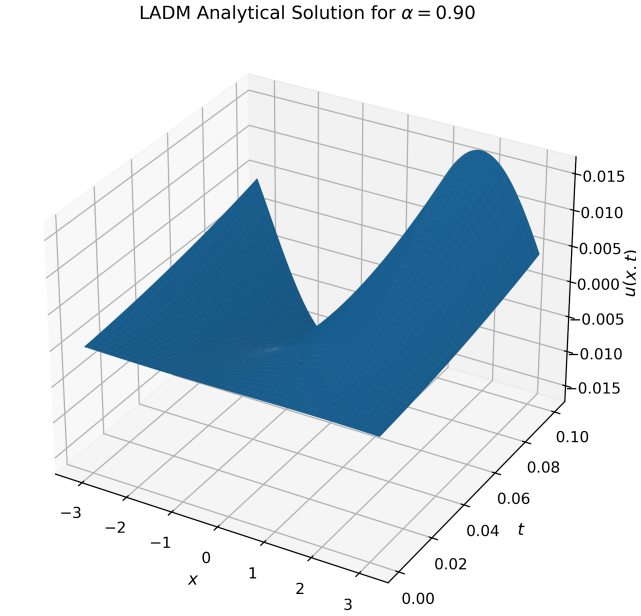


Fig. 2 Three-dimensional LADM solution for $\alpha = 0.90$ over the space–time domain.

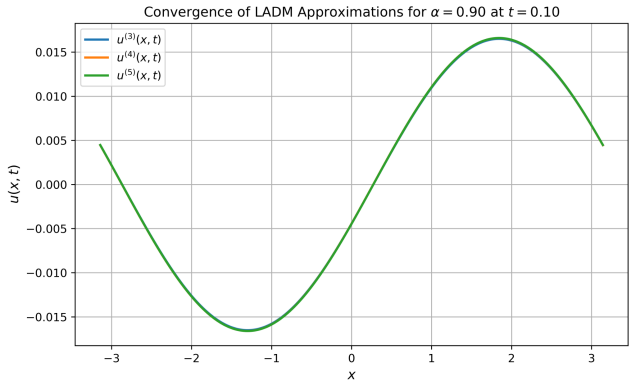


Fig. 3 Successive LADM approximations for $\alpha = 0.90$ at $t = 0.10$.

the forcing while the periodic spatial structure is preserved. The plotted surface is smooth through the initial transient. Figure 3 provides a visual comparison of the third-, fourth-, and fifth-order truncations. The curves are nearly indistinguishable at $t = 0.10$, consistent with the diagnostics in Table 1 and supporting the use of the six-component truncation in subsequent comparisons.

5 Numerical Application and Results

The numerical scheme of Section 3.2 is applied to the same benchmark, so that differences between the numerical and analytical approximations can be attributed to the solution methods under comparison.

5.1 Computational Setup

The numerical equation, domain, initial condition, and parameters are given in Eqs. (36)–(41). The spatial and temporal resolutions of the refined computation are

$$N_x = 128, \qquad N_t = 800, \tag{53}$$

and the coarser computation uses

$$N_x = 64, \qquad N_t = 400. \tag{54}$$

The pointwise difference between the numerical and LADM solutions is

$$E(x,t) = \left| u_{\mathrm{Num}}(x,t) - u_{\mathrm{LADM}}(x,t) \right|, \tag{55}$$

with relative L_2 error

$$E_{L_2} = \frac{\| u_{\mathrm{Num}} - u_{\mathrm{LADM}} \|_2}{\| u_{\mathrm{LADM}} \|_2}, \tag{56}$$

and maximum error

$$E_{\max} = \max_x \left| u_{\mathrm{Num}} - u_{\mathrm{LADM}} \right|. \tag{57}$$

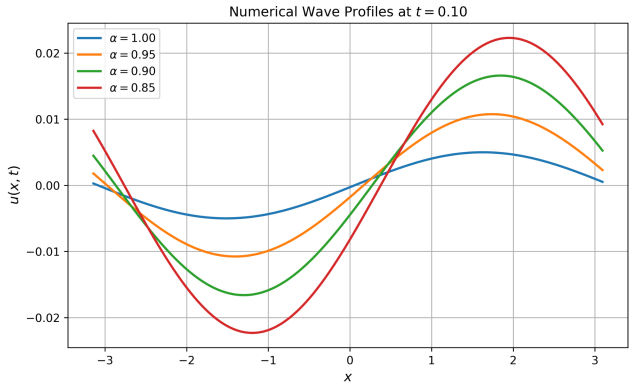


Fig. 4 Numerical wave profiles for different fractional orders at $t = 0.10$.

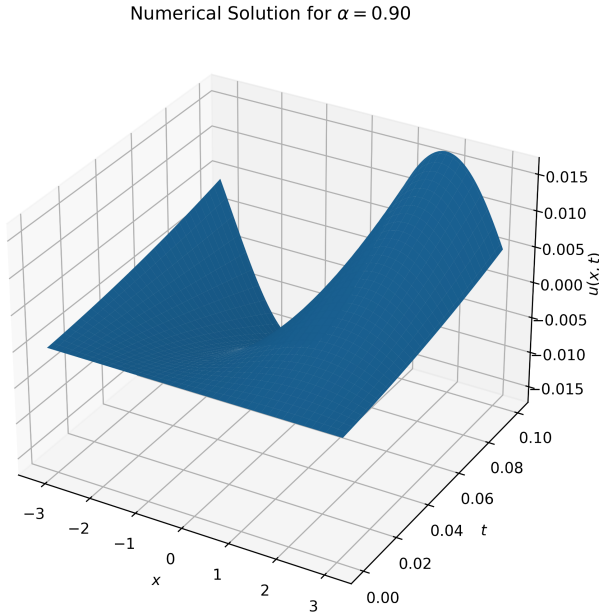


Fig. 5 Three-dimensional numerical solution for $\alpha = 0.90$ over the space–time domain.

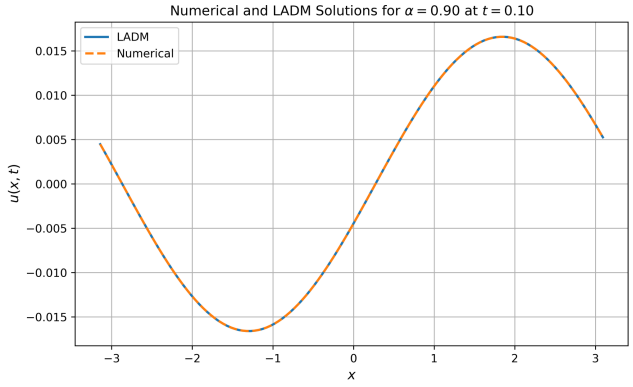


Fig. 6 Comparison between the numerical and six-component LADM solutions for $\alpha = 0.90$ at $t = 0.10$.

5.2 Numerical Results and Validation

Figure 4 reproduces the trend observed in the LADM solutions. Lower values of α lead to a stronger response under the same forcing. The three-dimensional numerical field in Figure 5 closely matches the analytical evolution in Figure 2. The solution starts from zero, remains smooth and periodic, and grows continuously over the selected time interval. For $\alpha = 0.90$, the numerical and analytical profiles in Figure 6 are visually indistinguishable over nearly the entire domain.

Table 2 Numerical-versus-LADM errors at $t = 0.10$.

α	Relative L_2 error	Maximum error
1.00	$4.42450475 \times 10^{-8}$	$2.21130576 \times 10^{-10}$
0.95	$1.14100547 \times 10^{-5}$	$1.27636378 \times 10^{-7}$
0.90	$3.21049038 \times 10^{-4}$	$5.65700071 \times 10^{-6}$
0.85	$2.91561950 \times 10^{-3}$	$7.04892195 \times 10^{-5}$

The numerical and LADM solutions agree closely for all four orders. At $\alpha = 0.90$, the relative L_2 difference is approximately 3.21×10^{-4}, or 0.0321%. Even at $\alpha = 0.85$, the relative error remains below 0.3%. The absolute-error

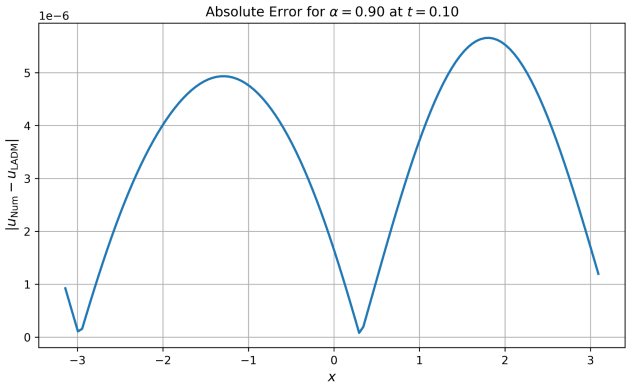


Fig. 7 Absolute difference between the numerical and LADM solutions for $\alpha = 0.90$ at $t = 0.10$.

profile in Figure 7 remains of order 10^{-6}. The error is largest in regions of high curvature and large amplitude, while its magnitude is several orders below that of the solution itself.

Table 3 Grid-refinement comparison between the 64×400 and 128×800 solutions.

α	Relative difference	Maximum difference
1.00	$1.32170402 \times 10^{-7}$	$6.60212680 \times 10^{-10}$
0.95	$7.46495903 \times 10^{-8}$	$8.03592498 \times 10^{-10}$
0.90	$5.63526560 \times 10^{-8}$	$9.37358500 \times 10^{-10}$
0.85	$4.64938066 \times 10^{-8}$	$1.04185851 \times 10^{-9}$

The relative grid-refinement differences in Table 3 range from order 10^{-8} to order 10^{-7}. For the lower fractional orders, these differences are several orders of magnitude smaller than the differences between the numerical and LADM solutions. This suggests that finite LADM truncation accounts for most of the discrepancy at those orders.

6 Physics-Informed Neural Network Application and Results

The PINN is applied to the representative fractional case $\alpha = 0.90$. The analytical and numerical results establish the fractional-order trend across four values of α. The PINN experiment tests whether a compact neural approximation can recover the fractional wave field from the governing physics. The predicted field is then compared with the refined numerical solution.

6.1 PINN Setup and Training Configuration

For $\alpha = 0.90$, the governing equation is

$$
\begin{aligned}
{}^{\mathrm{ABC}}D_t^{0.90}u + 2u_x + \frac{4}{7}uu_x - \frac{15}{7}u^2u_x \\
+ \frac{1}{3}u_{xxx} + \frac{1}{42}u_{xxxxx} = t\sin x.
\end{aligned}
\tag{58}
$$

The domain and initial condition are

$$
-\pi \le x \le \pi, \qquad 0 \le t \le 0.10, \qquad u(x,0) = 0. \tag{59}
$$

The network architecture is

$$
3 \longrightarrow 40 \longrightarrow 40 \longrightarrow 40 \longrightarrow 1, \tag{60}
$$

where the three inputs are $(\sin x, \cos x, t)$ and the output is the predicted wave amplitude. The hidden layers use hyperbolic tangent activation. The initial condition is imposed exactly through the transformed output

$$
\begin{aligned}
u_\theta(x,t) &= A_s \frac{t}{T}\widehat{u}_\theta(x,t), \\
A_s &= 0.03, \qquad T = 0.10.
\end{aligned}
\tag{61}
$$

Thus $u_\theta(x,0) = 0$ for all network parameters.

Table 4 PINN training configuration.

Quantity	Value
Fractional order	$\alpha = 0.90$
Spatial training points	$N_x = 20$
Temporal training points	$N_t = 21$
Hidden layers	3
Neurons per hidden layer	40
Activation	tanh
Optimizer	Adam
Learning rate	10^{-3}
Epochs	500
Floating-point precision	64-bit
Characteristic output scale	$A_s = 0.03$
Residual normalization scale	$U_s = 0.02$
Initial condition	Hard enforced
Spatial periodicity	$\sin x, \cos x$ encoding

With the adopted normalization, $B(0.90) = 0.9422008488$ and

$$
\frac{1-\alpha}{B(\alpha)} = 0.1061344830. \tag{62}
$$

The PINN right-hand side is

$$
\begin{aligned}
F_\theta = t\sin x - \Big[2(u_\theta)_x + \frac{4}{7}u_\theta(u_\theta)_x - \frac{15}{7}u_\theta^2(u_\theta)_x \\
+ \frac{1}{3}(u_\theta)_{xxx} + \frac{1}{42}(u_\theta)_{xxxxx} \Big].
\end{aligned}
\tag{63}
$$

The integral-form residual is

$$
\begin{aligned}
R_\theta = u_\theta - \frac{1-\alpha}{B(\alpha)}F_\theta \\
- \frac{\alpha}{B(\alpha)\Gamma(\alpha)} \int_0^t (t-\tau)^{\alpha-1} F_\theta(x,\tau)\,\mathrm{d}\tau,
\end{aligned}
\tag{64}
$$

and the optimized loss is the normalized mean-square residual

$$
\mathscr{L} = \frac{1}{N_f}\sum_{i=1}^{N_f} \left| \frac{R_\theta(x_i,t_i)}{0.02} \right|^2. \tag{65}
$$

Because the initial condition is imposed exactly, the initial-condition loss remains zero throughout training.

6.2 Training Convergence

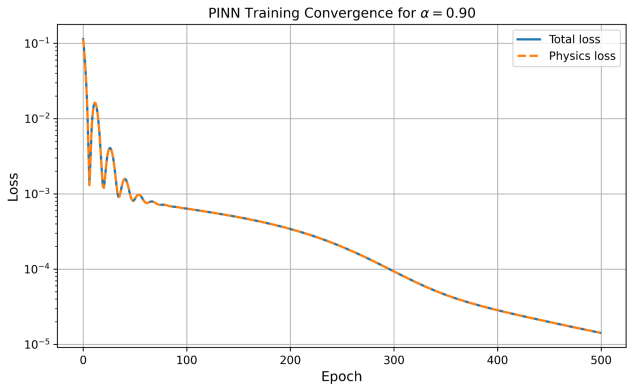


Fig. 8 PINN training-loss convergence for $\alpha = 0.90$.

The Adam training loss decreases from 1.140067×10^{-1} at the first epoch to approximately 1.426858×10^{-5} after 500 epochs. A final reevaluation gives

$$\mathscr{L}_{\text{final}} = 1.41754693 \times 10^{-5}, \qquad \mathscr{L}_{\text{IC}} = 0. \tag{66}$$

Figure 8 shows a steep initial reduction in the training loss followed by a slower, smooth decay. The loss shows no late-stage divergence despite the fifth-order spatial differentiation and the nonlocal time-history term.

6.3 PINN Validation Against the Numerical Solution

The trained PINN is evaluated on the 801×128 numerical reference grid generated in Section 5. The full space–time relative error is

$$E_{L_2}^{\text{ST}} = \frac{\|u_{\text{PINN}} - u_{\text{Num}}\|_2}{\|u_{\text{Num}}\|_2} = 1.07337185 \times 10^{-2}, \tag{67}$$

and the maximum space–time error is

$$E_{\max}^{\text{ST}} = 3.71971182 \times 10^{-4}. \tag{68}$$

At $t = 0.10$,

$$E_{L_2}^{t=0.10} = 1.25957586 \times 10^{-2}, \tag{69}$$

with

$$E_{\max}^{t=0.10} = 3.71971182 \times 10^{-4}. \tag{70}$$

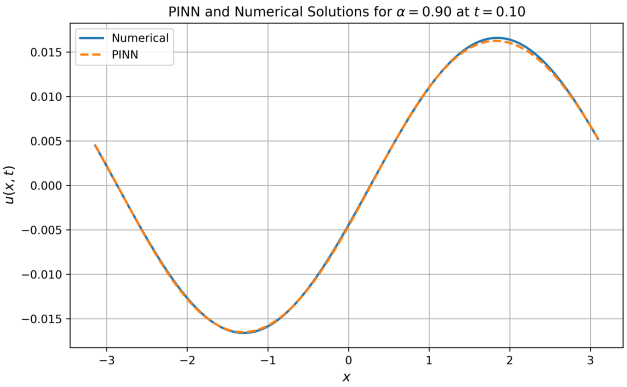


Fig. 9 Comparison between the PINN and numerical solutions for $\alpha = 0.90$ at $t = 0.10$.

The relative error is approximately 1.07% over the full space–time domain and 1.26% at the final time.

Figure 9 shows that the PINN captures both the negative trough and the positive crest of the numerical solution. The profiles remain close across the periodic interval, with the most visible discrepancy near the largest positive crest.

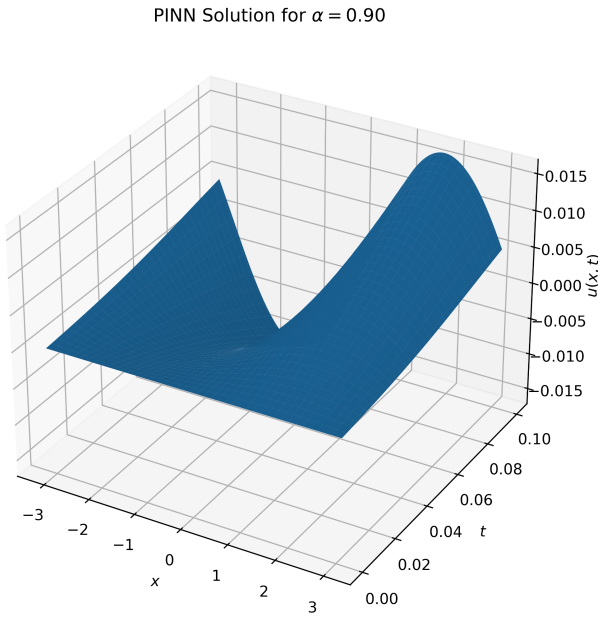


Fig. 10 Three-dimensional PINN solution for $\alpha = 0.90$ over the space–time domain.

The PINN surface in Figure 10 reproduces the overall space–time structure of the analytical and numerical solutions. The hard initial constraint makes the solution exactly

zero at $t = 0$, and the solution then grows smoothly under the forcing.

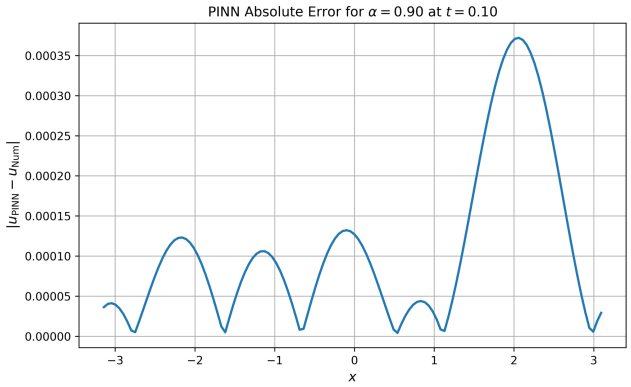


Fig. 11 Absolute PINN error relative to the numerical solution for $\alpha = 0.90$ at $t = 0.10$.

The final-time error profile in Figure 11 remains below 4×10^{-4}. The largest discrepancy occurs near the dominant positive crest, where the amplitude and spatial curvature are strongest.

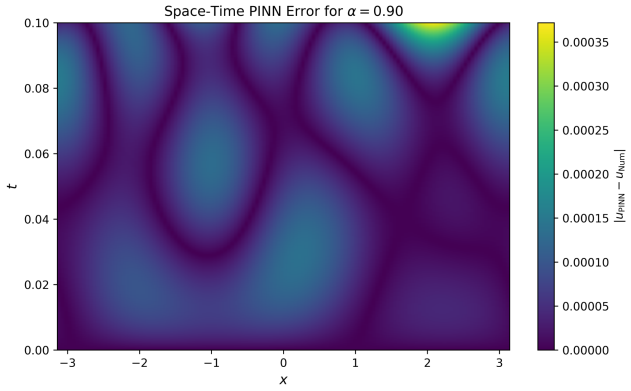


Fig. 12 Space–time absolute-error distribution between the PINN and numerical solutions for $\alpha = 0.90$.

The heat map in Figure 12 shows that the PINN error is smallest near the initial time and becomes more pronounced toward $t = 0.10$, especially around the growing crest. This pattern is consistent with the increasing difficulty of approximating the forced nonlinear wave as its amplitude grows. The error remains small compared with the solution scale across the domain.

7 Comparative Assessment of LADM, Numerical, and PINN Solutions

The three methods serve different mathematical roles. LADM provides an explicit truncated series that shows how forcing, nonlinearity, dispersion, and fractional memory enter successive corrections. The Fourier pseudospectral solver provides a numerical reference by resolving the periodic spatial derivatives spectrally. The grid-refinement test quantifies the sensitivity of that reference to the spatial and temporal resolutions tested. The PINN provides a global approximation constrained by the governing integral equation. For $\alpha = 0.90$, the relative difference between the numerical and LADM solutions at $t = 0.10$ is 3.21049×10^{-4}, whereas the relative difference between the coarse and refined numerical grids is 5.63527×10^{-8}. The difference between the two numerical grids is thus several orders of magnitude smaller than the numerical–LADM difference. The PINN has a full-domain relative error of 1.07337×10^{-2} and a final-time relative error of 1.25958×10^{-2} against the numerical reference. It reproduces the principal wave shape with a relative error of approximately 1% over the space–time domain.

The following comparisons bring together the fractional-order response, the full space–time surfaces, and the pairwise profiles and errors reported in Sections 4–6.

7.1 Fractional-Order Response Consistency

Figure 13 shows that the LADM and Fourier pseudospectral solutions predict the same dependence on the fractional order. At each tested value of α, the two profiles agree closely in phase and overall shape. In both computations, the amplitude increases as α decreases. The agreement between the two methods supports the interpretation that the stronger response arises from the ABC memory law.

7.2 Three-Way Space–Time Surface Comparison

The three surfaces in Figure 14 start from the zero initial state and show a periodic wave that grows under the forcing. The LADM and numerical surfaces are visually almost

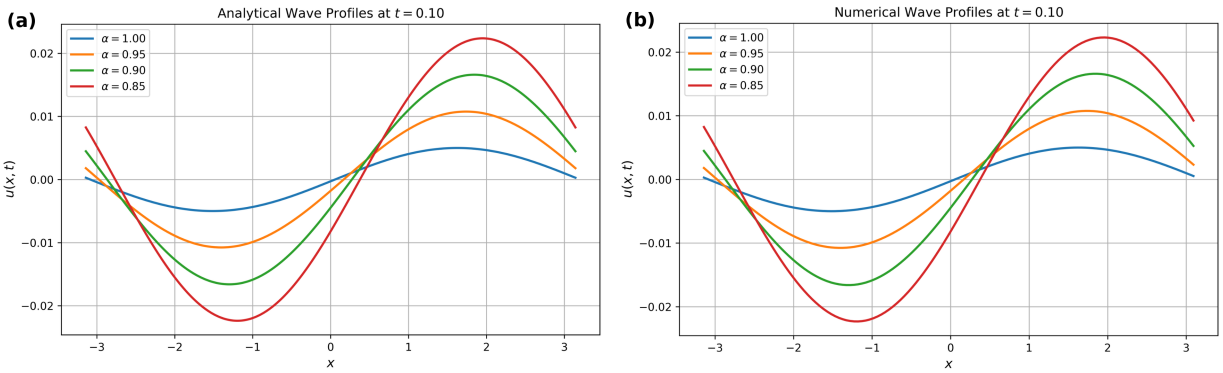


Fig. 13 Side-by-side LADM and numerical wave profiles for $\alpha = 1.00, 0.95, 0.90$, and 0.85 at $t = 0.10$.

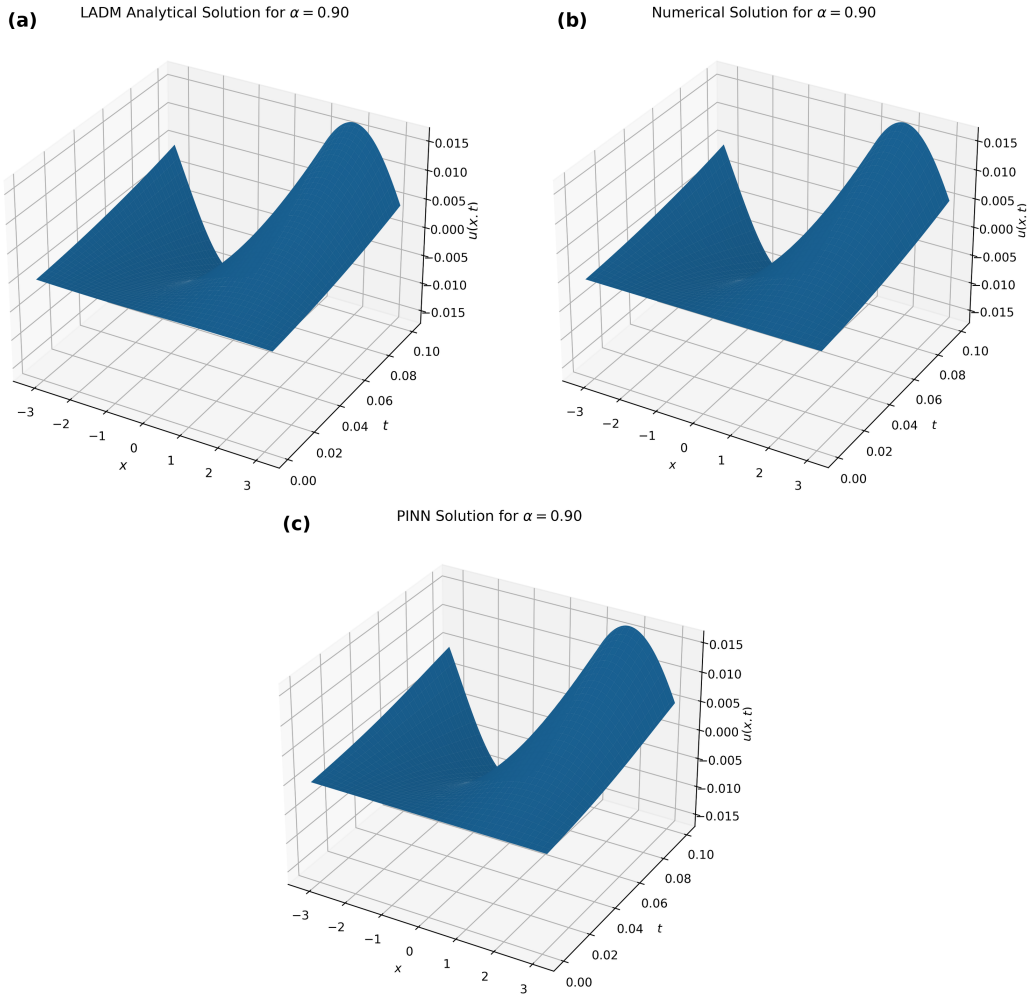


Fig. 14 Three-dimensional comparison for $\alpha = 0.90$. (a) LADM approximation, (b) Fourier pseudospectral solution, and (c) PINN reconstruction.

Table 5 Three-way comparison for the representative case $\alpha = 0.90$.

Method	Main representation	Key validation measure	Observed value	Principal strength	Main limitation
Six-component LADM	Semi-analytical series	Relative difference from the numerical solution at $t = 0.10$	3.21049×10^{-4}	Explicit analytical structure and close agreement between successive short-time truncations	Accuracy depends on the truncation and the time interval
Fourier pseudospectral with ABC history	Grid-based deterministic solution	Relative difference between the 64×400 and 128×800 grids	5.63527×10^{-8}	Small sensitivity to grid refinement in the present study	Requires grid-based time integration and storage and updating of the nonlocal history
PINN	Global neural approximation	Full space–time relative L_2 error against the numerical reference	1.07337×10^{-2}	Continuous approximation with the governing physics embedded in the loss	Training is slower and agreement with the numerical reference is weaker for this benchmark

indistinguishable, consistent with their small relative difference. The PINN reproduces the overall wave shape and the locations of the dominant crest and trough, with small amplitude deviations at later times. Table 5 quantifies the differences between the computed fields.

7.3 Pairwise Profile and Error Comparison

In Figure 15(a,c), the LADM and numerical curves overlap almost perfectly, with pointwise differences of order 10^{-6}. Panels (b) and (d) show that the PINN also reconstructs the wave profile, with a larger discrepancy that reaches approximately 3.72×10^{-4} near the dominant crest. The final-time relative L_2 differences are 3.21×10^{-4} for numerical versus LADM and 1.26×10^{-2} for PINN versus numerical. The spectral solution provides the numerical reference, the six-component LADM gives an accurate short-time analytical approximation, and the PINN provides a global surrogate constrained by the integral equation.

LADM is useful when a compact analytical series and interpretation of the parameters are important. The Fourier pseudospectral solver provides an accurate reference on the periodic domain. The PINN offers a reusable differentiable surrogate for extensions involving incomplete data or inverse problems. In this forward benchmark, the deterministic and analytical approximations agree closely, and the neural approximation is assessed against the refined numerical reference in addition to its training residual.

8 Comparison with Related Published Studies

We compare the present results with representative studies of fractional Kawahara-type models, classical GK computation, and PINN methods for high-order Kawahara equations. The governing equations, domains, initial data, fractional operators, and test cases vary across studies, so the comparison focuses on model scope, memory operator, methodology, and validation strategy.

The closest study involving fractional memory is that of Bhatter et al. [17], who used the ABC operator for a modified Kawahara equation and obtained analytical approximations through the homotopy analysis transform method (HATM). Their work illustrates the use of Mittag–Leffler memory in fifth-order nonlinear dispersive waves. The GK equation studied here retains both uu_x and u^2u_x. Its analytical approximation is compared with an independent pseudospectral history solver and used in a three-way assessment.

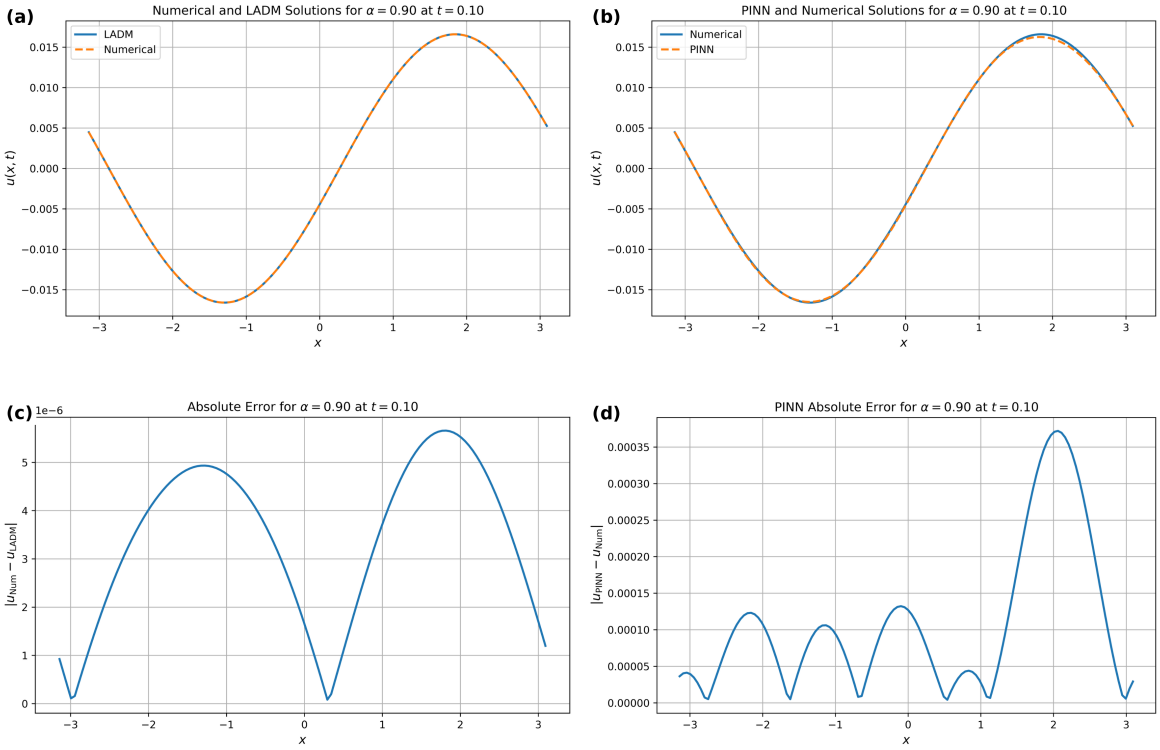


Fig. 15 Pairwise validation for $\alpha = 0.90$ at $t = 0.10$. (a) LADM versus numerical solution, (b) PINN versus numerical solution, (c) $|u_{\text{Num}} - u_{\text{LADM}}|$, and (d) $|u_{\text{PINN}} - u_{\text{Num}}|$.

Table 6 Position of the present study relative to representative literature.

Study	**Model/operator**	**Main method**	**Key distinction relative to the present work**
Bhatter et al. [17]	ABC fractional modified Kawahara equation	Homotopy analysis transform	Uses Mittag–Leffler memory for a modified Kawahara equation. The present study combines quadratic and cubic GK nonlinearities with a three-way comparison.
Ullah et al. [19]	Caputo fractional Kawahara and modified Kawahara equations	Integral transforms and decomposition	Uses the singular power-law Caputo kernel.
Ucar et al. [20]	Classical Gardner–Kawahara equation	Trigonometric quintic B-spline collocation	Treats integer-order GK dynamics.
Ali et al. [21]	Classical Gardner–Kawahara equation	Exact expansions and septic B-spline collocation	Compares exact and numerical results for the classical model.
Towhiduzzaman et al. [26]	$(3+1)$-dimensional Fornberg–Whitham equation	Hirota bilinear method and PINN	Compares analytical and PINN solutions using coordinated multi-panel visualizations.
Kabiri and Sabooni [27]	Classical Gardner–Kawahara inverse problem	PINN	Recovers unknown coefficients from sparse data.
Anand et al. [28]	Modified Kawahara equations	PINN with curriculum learning	Treats forward problems for modified Kawahara equations.

The classical GK studies by Ucar et al. [20] and Ali et al. [21] demonstrate the effectiveness of high-order B-spline collocation for integer-order GK dynamics. On the periodic domain considered here, the Fourier method evaluates spatial derivatives globally in spectral space. The relative grid-refinement differences in Table 3 are of order 10^{-8} to 10^{-7}, indicating low sensitivity to refinement for this test problem.

Towhiduzzaman et al. [26] combined Hirota-based analytical solutions with PINN reconstruction for a $(3+1)$-dimensional Fornberg–Whitham equation and used surface, contour, profile, and error plots to assess the learned wave structures. Kabiri and Sabooni [27] used a PINN to identify unknown coefficients from sparse data in inverse Gardner–Kawahara problems. Anand et al. [28] applied PINNs with curriculum learning to modified Kawahara equations. These studies show that neural networks can handle high-order dispersive operators. The present study incorporates nonlocal ABC temporal memory and adds an independent grid-converged Fourier benchmark. The PINN is thus evaluated against a numerical reference that can also be compared with the analytical approximation.

ABC fractional derivatives, decomposition methods, Fourier methods, GK solvers, and PINNs are all established in prior work. The central contribution of the present study is to bring these methods together in a compatibility-aware ABC Gardner–Kawahara benchmark and to compare the resulting analytical, numerical, and neural approximations.

9 Conclusion

We investigated a forced ABC fractional Gardner–Kawahara equation using Laplace–Adomian decomposition, a Fourier pseudospectral solver with ABC time integration, and a physics-informed neural network. The benchmark uses a zero initial state and a forcing term $t\sin x$ that vanishes at $t=0$. This choice satisfies the initial-time compatibility condition of the AB integral equation and avoids the start-up mismatch that can arise when the prescribed initial profile and the right-hand side are incompatible.

For the selected parameters on $0 \le t \le 0.10$, the six-component LADM approximation has a small last retained component and a small normalized integral residual. Even at $\alpha = 0.85$, the last component accounts for less than 1% of the accumulated solution magnitude, and the normalized residual is approximately 0.31%. As α decreases from 1.00 to 0.85, the forced transient grows in amplitude and changes modestly in shape. The Fourier pseudospectral results reproduce these trends. At $t = 0.10$, the relative numerical–LADM difference ranges from 4.42×10^{-8} at $\alpha = 1$ to 2.92×10^{-3} at $\alpha = 0.85$. The relative grid-refinement differences are of order 10^{-8} to 10^{-7}. For $\alpha = 0.90$, the relative numerical–LADM difference is 3.21×10^{-4}.

The PINN experiment provides a third comparison. A compact $3-40-40-40-1$ network uses periodic spatial features, hard enforcement of the zero initial condition, fifth-order automatic differentiation, and a residual based on the AB integral equation. Its final normalized training loss is approximately 1.42×10^{-5}. Against the refined numerical reference, the PINN yields a relative L_2 error of approximately 1.07% over the full space–time domain and 1.26% at the final time. It reconstructs the main wave features without using the numerical solution as training data.

For this benchmark, changing the ABC fractional order substantially alters the amplitude of the forced transient. The semi-analytical series shows how successive corrections enter the approximation, the spectral solver supplies a reference checked by grid refinement, and the PINN provides a continuous approximation constrained by the nonlocal integral equation.

Future work could extend the benchmark to longer times, nonzero initial states that satisfy the compatibility condition, alternative forcing functions, and physically calibrated parameter sets. Fast-history or sum-of-exponentials approximations could reduce the cost of evaluating the ABC memory term. Adaptive sampling, curriculum time marching, Fourier features, operator learning, and higher-order optimization could improve PINN accuracy or reduce training cost. The same framework could also be used to identify the fractional order and Gardner–Kawahara coefficients from sparse measurements.

References

1. I. Podlubny, *Fractional Differential Equations*, Academic Press, San Diego, 1999.
2. A. A. Kilbas, H. M. Srivastava, and J. J. Trujillo, *Theory and Applications of Fractional Differential Equations*, Elsevier, Amsterdam, 2006.
3. K. Diethelm, *The Analysis of Fractional Differential Equations*, Springer, Berlin, 2010. doi: 10.1007/978-3-642-14574-2.
4. M. Caputo, Linear models of dissipation whose Q is almost frequency independent—II, *Geophysical Journal of the Royal Astronomical Society* **13**(5), 529–539 (1967). doi: 10.1111/j.1365-246X.1967.tb02303.x.
5. A. Atangana and D. Baleanu, New fractional derivatives with nonlocal and non-singular kernel: Theory and application to heat transfer model, *Thermal Science* **20**(2), 763–769 (2016). doi: 10.2298/TSCI160111018A.
6. T. Abdeljawad and D. Baleanu, Integration by parts and its applications of a new nonlocal fractional derivative with Mittag–Leffler nonsingular kernel, *Journal of Nonlinear Sciences and Applications* **10**(3), 1098–1107 (2017). doi: 10.22436/jnsa.010.03.20.
7. S. Yadav, R. K. Pandey, and A. K. Shukla, Numerical approximations of Atangana–Baleanu Caputo derivative and its application, *Chaos, Solitons & Fractals* **118**, 58–64 (2019). doi: 10.1016/j.chaos.2018.11.009.
8. A. Atangana and K. M. Owolabi, New numerical approach for fractional differential equations, *Mathematical Modelling of Natural Phenomena* **13**(1), 3 (2018). doi: 10.1051/mmnp/2018010.
9. S. Aljhani, M. S. M. Noorani, R. Douaifia, and S. Abdelmalek, A high-order predictor–corrector method for initial value problems with fractional derivative involving Mittag–Leffler kernel, *Mathematical Methods in the Applied Sciences* **48**(7), 7378–7397 (2025). doi: 10.1002/mma.9040.
10. K. Diethelm, N. J. Ford, and A. D. Freed, A predictor–corrector approach for the numerical solution of fractional differential equations, *Nonlinear Dynamics* **29**, 3–22 (2002). doi: 10.1023/A:1016592219341.
11. T. Kawahara, Oscillatory solitary waves in dispersive media, *Journal of the Physical Society of Japan* **33**(1), 260–264 (1972). doi: 10.1143/JPSJ.33.260.
12. O. Kurkina, N. Singh, and Y. Stepanyants, Structure of internal solitary waves in two-layer fluid at near-critical situation, *Communications in Nonlinear Science and Numerical Simulation* **22**, 1235–1242 (2015). doi: 10.1016/j.cnsns.2014.09.018.
13. N. Polat, D. Kaya, and H. I. Tutalar, A analytic and numerical solution to a modified Kawahara equation and a convergence analysis of the method, *Applied Mathematics and Computation* **181**(1), 193–199 (2006). doi: 10.1016/j.amc.2005.11.104.
14. D. Kaya and K. Al-Khaled, A numerical comparison of a Kawahara equation, *Physics Letters A* **363**(5–6), 433–439 (2007). doi: 10.1016/j.physleta.2006.11.055.
15. M. Benbachir and A. Saadi, The Kawahara equation with time and space-fractional derivatives solved by the Adomian method, *Journal of Interdisciplinary Mathematics* **17**(3), 243–253 (2014). doi: 10.1080/09720502.2013.801657.
16. A. Atangana, N. Bildik, and S. C. O. Noutchie, New iteration methods for time-fractional modified nonlinear Kawahara equation, *Abstract and Applied Analysis* **2014**, 740248 (2014). doi: 10.1155/2014/740248.
17. S. Bhatter, A. Mathur, D. Kumar, K. S. Nisar, and J. Singh, Fractional modified Kawahara equation with Mittag–Leffler law, *Chaos, Solitons & Fractals* **131**, 109508 (2020). doi: 10.1016/j.chaos.2019.109508.
18. A. Daşcıoğlu and S. Çulha Ünal, New exact solutions for the space-time fractional Kawahara equation, *Applied Mathematical Modelling* **89**, 952–965 (2021). doi: 10.1016/j.apm.2020.07.053.
19. I. Ullah, A. Ali, and S. Saifullah, Analysis of time-fractional non-linear Kawahara equations with power law kernel, *Chaos, Solitons & Fractals: X* **9**, 100084 (2022). doi: 10.1016/j.csfx.2022.100084.
20. Y. Ucar, N. M. Yagmurlu, A. Esen, and B. Karaagac, A new numerical approach to Gardner Kawahara equation in magneto-acoustic waves in plasma physics, *International Journal for Numerical Methods in Fluids* **95**(6),

979–991 (2023). doi: 10.1002/fld.5181.

21. K. K. Ali, D. Yıldırım Sucu, and S. B. G. Karakoc, Two effective methods for solution of the Gardner–Kawahara equation arising in wave propagation, *Mathematics and Computers in Simulation* **220**, 192–203 (2024). doi: 10.1016/j.matcom.2024.01.005.
22. Y. Gong, J. Cai, and Y. Wang, Multi-symplectic Fourier pseudospectral method for the Kawahara equation, *Communications in Computational Physics* **16**(1), 35–55 (2014). doi: 10.4208/cicp.090313.041113a.
23. M. Raissi, P. Perdikaris, and G. E. Karniadakis, Physics-informed neural networks: A deep learning framework for solving forward and inverse problems involving nonlinear partial differential equations, *Journal of Computational Physics* **378**, 686–707 (2019). doi: 10.1016/j.jcp.2018.10.045.
24. G. Pang, L. Lu, and G. E. Karniadakis, fPINNs: Fractional physics-informed neural networks, *SIAM Journal on Scientific Computing* **41**(4), A2603–A2626 (2019). doi: 10.1137/18M1229845.
25. G. E. Karniadakis, I. G. Kevrekidis, L. Lu, P. Perdikaris, S. Wang, and L. Yang, Physics-informed machine learning, *Nature Reviews Physics* **3**, 422–440 (2021). doi: 10.1038/s42254-021-00314-5.
26. M. Towhiduzzaman, M. A. Al Mohit, and A. Z. M. Asaduzzaman, Modeling lump and soliton wave interactions in the $(3+1)$D Fornberg–Whitham equation using a physics-informed neural network framework, *Partial Differential Equations in Applied Mathematics* **17**, 101330 (2026). doi: 10.1016/j.padiff.2025.101330.
27. M. Kabiri and S. Sabooni, Solving inverse Gardner–Kawahara problems with physics-informed neural networks: A data-driven approach, *Physica Scripta* **100**(10), 105204 (2025). doi: 10.1088/1402-4896/ae0769.
28. S. Anand, S. Natesan, and Ş. Toprakseven, Physics informed neural network framework for modified Kawahara equations, *Advances in Computational Science and Engineering* **8**, 50–73 (2026). doi: 10.3934/acse.2026007.